Theory of Infrared Microspectroscopy for Intact Fibers

Brynmor J. Davis,[†,§] **P. Scott Carney,**[‡] **and Rohit Bhargava**[*,§]

Department of Bioengineering, Department of Electrical and Computer Engineering, and The Beckman Institute for Advanced Science and Technology, University of Illinois at Urbana–Champaign, Urbana, Illinois, United States

Infrared microspectroscopy is widely used for the chemical analysis of small samples. In particular, spectral properties of small cylindrical samples are important in forensic analysis, understanding relationships between microstructure and mechanical properties in fibers or fiber composites, and development of cosmetics and drugs for hair. The diameters of the constituent cylinders are typically of the order of the central wavelength of light used to probe the sample. Hence, structure and material spectral response are coupled and recorded spectra are usually distorted to the extent of becoming useless for molecular identification. In this paper, we apply rigorous optical theory to predict the spectral distortions observed in IR microspectroscopic data of fibers. The theory is used, first, to compute the changes that are observed for cylinders of various dimensions under different instrument configurations when compared to the bulk spectrum from the same material. We provide a method to recover intrinsic material spectral response from fibers by correcting for distortion introduced by the cylindrical structure. The theory reported here should enable the routine use of IR microspectroscopy and imaging for the molecular analysis of cylindrical domains in complex materials.

Infrared (IR) vibrational spectroscopy has been extensively used in the molecular analysis of fibers,[1,2] hair, and for composites with fiber-type inclusions.[3–6] For synthetic fibers, IR spectra provide molecular, microstructural and orientation measurements used in predicting the mechanical properties of the sample. Since these properties of the fiber determine its suitability for specific applications, the accuracy of spectroscopic measurements is critical. Accurate spectral information is also critical for the analysis of fiber-type samples of forensic interest, for example synthetic and natural fibers as well as hair. A rapid and convenient method to characterize these samples is infrared (IR) absorption spectroscopy in which the vibrational spectrum of a material can potentially be used to determine the above properties of interest. Given the small size of individual fibers, a microspectrometric[7] measurement is usually conducted.[8,9] Direct recording of spectral data from fibers leads to extensive distortions in the spectra as compared to the intrinsic material response.[10,11] The sample refracts light, acting as a lens, and also scatters light, thereby complicating the otherwise simple equivalence of the geometrical parameters of the sample and effective path length to be used for quantitative analysis in Beer's law. More importantly, the diameter of fibers is often of the same order of magnitude as the wavelength of light in the mid-IR. Hence, wavelength-dependent scattering at the sample boundary imparts a molecularly nonspecific attenuation that complicates interpretation of the data.[12] The effect of these spectral distortions can be gauged in contrasting the rather limited progress in IR spectroscopic analysis of fibrous materials with that achieved, in both theory and practice, using Raman microspectroscopic analysis.[13] To overcome spectral distortions and enable IR spectral analyses, the use of alternatives such as microtoming,[14,15] solution casting, sample flattening,[16] the use of a diamond anvil cell[17] or the use of other spectroscopic techniques[18] is prescribed. These methods, however, are suboptimal as they often destroy some structure of the fibers that may be useful for forensic analysis[19] or for relating fiber structures to their properties.

We recently developed a rigorous optical theory for infrared microspectroscopy in which a framework was proposed to relate the recorded spectroscopic imaging data to the experimental setup

* To whom correspondence should be addressed. E-mail: rxb@illinois.edu.
† Current affiliation: Creare Inc., P.O. Box 71, Hanover, NH 03755.
‡ Department of Electrical and Computer Engineering, and the Beckman Institute.
§ Department of Bioengineering and the Beckman Institute.

(1) O'Connor, R. T.; DuPré, E. F.; Mitcham, D. *Text. Res. J.* **1958**, *382–392*, 1958.
(2) Murthy, N. S.; Bray, R. G.; Correale, S. T.; Moore, R. A. F. *Polymer* **1995**, *36*, 3863–3873.
(3) Felix, J. M.; Gatenholm, P. *J. Appl. Polym. Sci.* **1991**, *42*, 609–620.
(4) Ishida, H.; Koenig, J. L. *Polym. Eng. Sci.* **1978**, *18*, 128–145.
(5) Bhargava, R.; Wang, S. Q.; Koenig, J. L. *Adv. Polym. Sci.* **2003**, *163*, 137–191.
(6) Compton, S.; Powell, J. *Am. Lab.* **1991**, *23*, 41–51.
(7) Levin, I. W.; Bhargava, R. *Annu. Rev. Phys. Chem.* **2005**, *56*, 429–474.
(8) Fox, R. H.; Schuetzman, H. I. *J. Forensic Sci.* **1968**, *13*, 397.
(9) Tungol, M. W.; Bartick, E. G.; Montaser, A. *Appl. Spectrosc.* **1990**, *44*, 543–549.
(10) Tungol, M. W.; Bartick, E. G.; Montaser, A. *J. Forensic Sci.* **1991**, *36*, 1027–1043.
(11) Flynn, K.; O'Leary, R.; Roux, C.; Reedy, B. J. *J. Forensic Sci.* **2006**, *51*, 586–596.
(12) Martoglio, P. A.; Bouffard, S. P.; Sommer, A. J.; Katon, J. E.; Jakes, K. A. *Anal. Chem.* **1990**, *62*, 1123A–1128A.
(13) Sourisseau, C. *Chem. Rev.* **2004**, *104*, 3851–3891.
(14) Kalasinsky, K. S.; Magluilo, J., Jr.; Schaefer, T. *Forensic Sci. Int.* **1993**, *63*, 253–260.
(15) Bantignies, J. L.; Fuchs, G.; Carr, G. L.; Williams, G. P.; Lutz, D.; Marull, S. *J. Cosmet. Sci.* **2000**, *51*, 73–90.
(16) Bartick, E. G.; Tungol, M. W.; Reffner, J. A. *Anal. Chim. Acta* **1994**, *288*, 35–42.
(17) Read, L. K.; Kopec, R. J. *J.−Assoc. Off. Anal. Chem.* **1978**, *61*, 526.
(18) Miller, J. V.; Bartick, E. G. *Appl. Spectrosc.* **2001**, *55*, 1729–1732.
(19) Cho, L.; Reffner, J. A.; Wetzel, D. A. *J. Forensic Sci.* **1999**, *44*, 283–291.

and sample properties.[20,21] Theoretical predictions and experimental validation demonstrated that spectral distortions could be modeled for simple geometries such as layered samples or simple edges. Here, we extend the theory to cylindrical objects to understand spectral distortions in fibers. Correction of distortions using the developed theoretical treatment can enable truly nonperturbing IR microspectroscopic analysis. We do not explicitly address polarization and dichroic or trichroic ratio measurements here and restrict discussion to isotropic fibers. Nevertheless, the developed framework can be extended to extract these measures of orientation as well.

First, classical optical theory is used to describe the interaction of focused light with a fiber with known radius and optical properties. For simplicity, scalar optical fields are used in this analysis but it should be understood that the method can be readily generalized to vector fields. Similarly, a homogeneous fiber is considered but the method used can be generalized, in a straightforward manner, to encompass multicore fibers, that is, fibers consisting of concentric cylinders of different materials.

The forward model allows the prediction of measurements given a fiber with a material of known spectral properties and geometry. However, the goal of this work is to provide a means of determining the optical material properties from measurements. To do this an inverse problem must be solved—that is, given measurements, material properties are determined using the physical understanding of the system quantified by the forward model. Finally, a means of solving the inverse problem and an algorithmic implementation are described.

FORWARD MODEL

To understand the relationship between the collected data and the optical properties of the fiber material, it is necessary to understand the interaction of the optical fields in the measurement system with the fiber. The geometry of this system is illustrated in Figure 1. In this section the field incident on the fiber, the field in the fiber and the field scattered from the fiber will all be described. Using these fields, measurements can be predicted for a known fiber. This model is based on classical electromagnetic theory[22] and an appropriate detection model.[20]

General Form of the Optical Field. There are two regions of homogeneous material in this problem. It is convenient to represent the total field U differently in each region, that is,

$$U(\theta, \rho, y, \bar{\nu}) = \begin{cases} U_0(\theta, \rho, y, \bar{\nu}) = U_i(\theta, \rho, y, \bar{\nu}) + U_s(\theta, \rho, y, \bar{\nu}) & \rho > R \\ U_1(\theta, \rho, y, \bar{\nu}) & \rho \leq R \end{cases} \quad (1)$$

where R is the radius of the fiber and $\bar{\nu}$ is the wavenumber (the reciprocal of the wavelength). Here U_0 describes the field outside the fiber, while U_1 describes the internal field. Further, the external field is the superposition of U_i, the field used to illuminate the fiber, and U_s, the field scattered from the fiber.

The optical properties of each region are determined by a complex refractive index. The region outside the fiber is assumed to be air, with a refractive index well approximated as unity. The
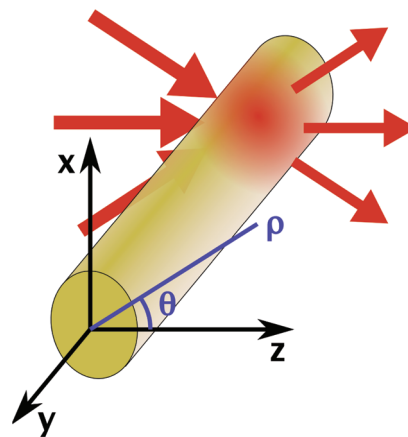
(20) Davis, B. J.; Carney, P. S.; Bhargava, R. *Anal. Chem.* **2010**, *82*, 3487–3499.
(21) Davis, B. J.; Carney, P. S.; Bhargava, R. *Anal. Chem.* **2010**, *82*, 3474–3486.
(22) van de Hulst, H. C., *Light Scattering by Small Particles*, Chapter 15; Dover: Mineola, NY, 1981.

Figure 1. Illustration of the system considered. Light is focused on to a fiber of fixed radius with the goal of obtaining measurements that can be used to determine the optical properties of the fiber material. The analysis used to describe this system employs both Cartesian and cylindrical coordinates, as shown. The axis of the fiber is chosen to lie along the *y* axis of both coordinate systems. The distance from the origin, $r = (x^2 + y^2 + z^2)^{1/2} = (\rho^2 + y^2)^{1/2}$, also appears in the resulting expressions.

fiber has a complex refractive index $n(\bar{\nu}) + ik(\bar{\nu})$, with the imaginary part $k(\bar{\nu})$ determining absorption properties. The fields in the system are found by using well-known representations of fields in homogeneous materials and ensuring that boundary conditions are satisfied at the interface of the fiber and the surrounding air.

Optical Fields in Cylindrical Coordinates. As illustrated in Figure 1, the symmetry of the fiber suggests an analysis in cylindrical coordinates. For this reason, all relevant optical fields will be represented in (θ, ρ, y) coordinates and converted to Cartesian coordinates where required. In cylindrical coordinates, fields in a homogeneous medium can be written in terms of the modal expansion[22]

$$U_h(\theta, \rho, y, \bar{\nu}) = \sum_{m=-\infty}^{\infty} \int ds_y G_h(m, s_y, \bar{\nu}) e^{im\theta} \times Z_m\{2\pi\bar{\nu}\rho\sqrt{[n(\bar{\nu}) + ik(\bar{\nu})]^2 - s_y^2}\}\exp(i2\pi\bar{\nu}s_y y) \quad (2)$$

based on the solutions to the wave equation found via separation of variables. Here Z_m is a Bessel function of order m and can represent either Bessel functions of the first kind, J_m, or Bessel functions of the second kind, Y_m. The function $G_h(m, s_y, \bar{\nu})$ represents coefficients of the cylindrical Bessel modes and can be thought of as a spectral representation of the homogeneous-material field $U_h(\theta, \rho, y, \bar{\nu})$. In eq 2, the general refractive index $n(\bar{\nu}) + ik(\bar{\nu})$ appears in the argument of the Bessel function. In air, this quantity is replaced by 1.

The Illuminating Field. The fiber is illuminated by light from a focusing system, typically a Cassegrain reflector. In this treatment, the optical axis of the focusing system is assumed to be perpendicular to the fiber and is assigned to the *z* axis. A focused field is most typically described in Cartesian coordinates as $\tilde{U}_i(x, y, z, \bar{\nu})$, where a tilde will be used to denote a function on Cartesian axes.

The focused field is conveniently described using an angular spectrum of planewaves.[23]

$$\tilde{U}_i(x, y, z, \bar{\nu}) =$$
$$i\bar{\nu} \iint ds_x ds_y \frac{\tilde{B}_i(s_x, s_y, \bar{\nu})}{s_z} \exp[i2\pi\bar{\nu}(s_x x + s_y y + s_z z)] \quad (3)$$

where

$$s_z = \sqrt{1 - s_x^2 - s_y^2} \quad (4)$$

Here the unit vector (s_x, s_y, s_z) gives the direction of propagation of each planewave component and $\tilde{B}_i(s_x, s_y, \bar{\nu})$ is the planewave angular spectrum of the illuminating field.

The modal expansion of eq 3 is defined such that the field at large distances r from the origin is $\tilde{B}_i(x/r, y/r, \bar{\nu})e^{i2\pi\bar{\nu}r}/r$ for positive values of z and $-\tilde{B}_i(x/r, y/r, \bar{\nu})e^{i2\pi\bar{\nu}r}/r$ for negative values z. The field on the hemisphere of the illuminating aperture (which lies in the $-z$ half space) is therefore proportional to the angular spectrum of the illuminating field. In this scalar treatment, the field across the illuminating aperture is taken to be constant so that

$$\tilde{B}_i(s_x, s_y, \bar{\nu}) = \begin{cases} 1 & \Gamma_1 \geq \sqrt{s_x^2 + s_y^2} \geq \Gamma_2 \\ 0 & \text{else} \end{cases} \quad (5)$$

where Γ_2 is the numerical aperture of the Cassegrain and Γ_1 is the numerical aperture of the central Cassegrain obstruction.

As mentioned earlier, it will be convenient to represent the illuminating field in cylindrical coordinates. It is therefore necessary to make the coordinate transformation $(x, y, z) \Rightarrow (\rho, \theta, y)$, which results in the following transformation of the unit propagation vector

$$s_x = \sqrt{1 - s_y^2} \sin s_\theta \quad (6)$$

$$s_y = s_y \quad (7)$$

$$s_z = \sqrt{1 - s_y^2} \cos s_\theta \quad (8)$$

The Cartesian angular spectrum representation of eq 3 then becomes

$$U_i(\theta, \rho, y, \bar{\nu}) =$$
$$i\bar{\nu} \iint ds_\theta ds_y B_i(s_\theta, s_y, \bar{\nu}) \exp\{i2\pi\bar{\nu}[\rho\sqrt{1 - s_y^2} \cos(\theta - s_\theta) + s_y y]\} \quad (9)$$

It will be necessary to put this equation in the form of eq 2. This transformation can be achieved using the Jacobi-Anger expansion[24]

(23) Richards, B.; Wolf, E. *Proc. R. Soc. London, Ser. A* **1959**, *253*, 358–379.
(24) Cuyt, A. Petersen, V. Verdonk, B. Waadeland, H., Jones, W. B., *Handbook of Continued Fractions for Special Functions*; Springer: New York, 2008; p 344.
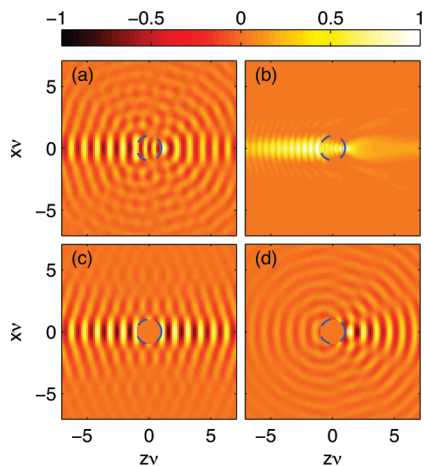
$$\exp(i2\pi\bar{\nu}\rho\sqrt{1 - s_y^2}\cos\theta) = \sum_{m=-\infty}^{\infty} i^m e^{im\theta} J_m(2\pi\bar{\nu}\rho\sqrt{1 - s_y^2}) \quad (10)$$

The illuminating field can be written in the form of eq 2 by substituting eq 10 into eq 9,

$$U_i(\theta, \rho, y, \bar{\nu}) = i\bar{\nu} \sum_{m=-\infty}^{\infty} \iint ds_y ds_\theta B_i(s_\theta, s_y, \bar{\nu}) e^{-ims_\theta} i^m e^{im\theta} \times$$
$$J_m(2\pi\bar{\nu}\rho\sqrt{1 - s_y^2}) \exp(i2\pi\bar{\nu}s_y y)$$
$$= \sum_{m=-\infty}^{\infty} \int ds_y G_i(m, s_y, \bar{\nu}) e^{im\theta} J_m(2\pi\bar{\nu}\rho\sqrt{1 - s_y^2}) \times$$
$$\exp(i2\pi\bar{\nu}s_y y) \quad (11)$$

with

$$G_i(m, s_y, \bar{\nu}) = i^{m+1}\bar{\nu} \int ds_\theta B_i(s_\theta, s_y, \bar{\nu}) e^{-ims_\theta} \quad (12)$$

Note that the expression above is closely related to the Fourier series of $B_i(s_\theta, s_y, \bar{\nu})$ over s_θ.

The Scattered and Internal Fields. The field inside the fiber can be expressed as in eq 2. In this case,

$$U_1(\theta, \rho, y, \bar{\nu}) = \sum_{m=-\infty}^{\infty} \int ds_y G_1(m, s_y, \bar{\nu}) e^{im\theta} \times$$
$$J_m\{2\pi\bar{\nu}\rho\sqrt{[n(\bar{\nu}) + ik(\bar{\nu})]^2 - s_y^2}\} \exp(i2\pi\bar{\nu}s_y y) \quad (13)$$

Here Bessel functions of the second kind, Y_m, are not included in the representation, as these functions are infinite at the origin and thus are nonphysical.

Similarly, the scattered field can be written as,

$$U_s(\theta, \rho, y, \bar{\nu}) = \sum_{m=-\infty}^{\infty} \int ds_y G_s(m, s_y, \bar{\nu}) e^{im\theta} \times$$
$$H_m(2\pi\bar{\nu}\rho\sqrt{1 - s_y^2}) \exp(i2\pi\bar{\nu}s_y y) \quad (14)$$

Here H_m is a Hankel function of the first kind, that is, $H_m(l) = J_m(l) + iY_m(l)$. This choice of Bessel function is made because Hankel functions represent strictly out-going waves, a condition required for the scattered field. Also note that the refractive index appearing in the argument of the Hankel function is unity, as the scattered field is in free space.

Solving for the Fields. It can be seen from eq 11, eq 13, and eq 14 that the illumination, internal and scattered fields can all be represented as a superposition of modal fields indexed by m and s_y. Each scattered mode and each internal mode is a solution of the wave equation and must be linearly related to the corresponding illumination mode. Consequently,

$$G_s(m, s_y, \bar{\nu}) = G_i(m, s_y, \bar{\nu}) a(m, s_y, \bar{\nu}) \quad (15)$$

$$G_1(m, s_y, \bar{\nu}) = G_i(m, s_y, \bar{\nu}) b(m, s_y, \bar{\nu}) \quad (16)$$

Figure 2. Illustration of the fields in and around a fiber when it is illuminated (from left to right) by a field focused to the center of the fiber by a Cassegrain: (a) the real part of the complex field $U(\theta, \rho, y, \bar{\nu})$; (b) the optical intensity of the field, that is, $|U(\theta, \rho, y, \bar{\nu})|^2$; (c) the real part of the complex field incident from the focusing Cassegrain $U_i(\theta, \rho, y, \bar{\nu})$; (d) the real part of the scattered field $U_s(\theta, \rho, y, \bar{\nu})$. In each case the x–z plane through the geometric focus is shown. The fiber (boundary indicated by the dashed blue line) has a radius of one wavelength and a refractive index of $1.45 + i0.025$. The numerical aperture of the Cassegrain is 0.4 and the numerical aperture of the obscuration is 0.1.

Additionally, the superposition of the illuminating, scattered and internal fields must be continuous and have a continuous first derivative. Therefore by considering the fields at the fiber boundary, $\rho = R$, the relationship between the illuminating field and the scattered and internal fields can be determined.

$$a(m, s_y, \bar{\nu}) =$$

$$\frac{\sqrt{[n(\bar{\nu}) + ik(\bar{\nu})]^2 - s_y^2} J_m(l_0) J'_m(l_1) - \sqrt{1 - s_y^2} J_m(l_1) J'_m(l_0)}{\sqrt{1 - s_y^2} J_m(l_1) H'_m(l_0) - \sqrt{[n(\bar{\nu}) + ik(\bar{\nu})]^2 - s_y^2} H_m(l_0) J'_m(l_1)}$$

(17)

$$b(m, s_y, \bar{\nu}) =$$

$$\frac{\sqrt{1 - s_y^2} J_m(l_0) H'_m(l_0) - \sqrt{1 - s_y^2} H_m(l_0) J'_m(l_0)}{\sqrt{1 - s_y^2} J_m(l_1) H'_m(l_0) - \sqrt{[n(\bar{\nu}) + ik(\bar{\nu})]^2 - s_y^2} H_m(l_0) J'_m(l_1)}$$

(18)

where $l_0 = 2\pi\bar{\nu}R(1 - s_y^2)^{1/2}$ and $l_1 = 2\pi\bar{\nu}R([n(\bar{\nu}) + ik(\bar{\nu})]^2 - s_y^2)^{1/2}$. The derivatives of the Bessel functions can be calculated using the property $Z'_m(l) = (m/l)Z_m(l) - Z_{m+1}(l)$. It can also be seen that $a(m, s_y, \bar{\nu}) = a(-m, s_y, \bar{\nu})$ and $b(m, s_y, \bar{\nu}) = b(-m, s_y, \bar{\nu})$, as $Z_{-m}(l) = (-1)^m Z_m(l)$.

The results above provide a means to calculate the fields resulting from the focused illumination of a fiber. An example is shown in Figure 2. It can be seen that the calculated fields sum to give a continuous field distribution. The scattered field (d) is concentrated in the forward scattering direction. This scattered field has the effect of canceling some of the field that would be

observed without the presence of the fiber (c). Physically, this cancellation accounts for the light extinguished by the fiber.[25]

Scattered Light in the Far-Field. The physical properties of the fiber are encoded in the scattered field, which is described by eq 14, eq 15, and eq 17. The integrand seen in eq 14 becomes highly oscillatory for large values of $\bar{\nu}\rho$, that is, as the field is evaluated a large number of wavelengths from the fiber. Thus asymptotic evaluation of eq 14 at the detection optics is sensible and is accomplished using the large-argument form of the Hankel function, $H_m(l) \sim (-i)^m ((2)/(i\pi l))^{1/2} \exp(il)$. Combining eq 14, eq 15, recalling eq 12 and applying the Fourier series convolution theorem gives a highly oscillatory complex exponential in the integrand that can be evaluated using the principle of stationary phase.[26] The resulting expression for the scattered field many wavelengths from the fiber is

$$\lim_{r\to\infty} U_s(\theta, \rho, y, \bar{\nu}) = \int ds_\theta B_i\left(s_\theta, \frac{y}{r}, \bar{\nu}\right) \alpha\left(\theta - s_\theta, \frac{y}{r}, \bar{\nu}\right) \frac{e^{i2\pi\bar{\nu}r}}{r}$$

(19)

where

$$\alpha(s_\theta, s_y, \bar{\nu}) = \frac{1}{\pi} \sum_{m=-\infty}^{\infty} a(m, s_y, \nu) e^{im\theta}$$

(20)

This expression is readily evaluated by numerical methods.

The Detected Signal. It will be assumed that an optical detection system is positioned in the far field of the $z \geq 0$ half space. Recall that the illuminating field is $B_i(\theta, y/r, \bar{\nu})\exp(i2\pi\bar{\nu}r)/r$ in this region. Consequently, the total field in the far field of the $z \geq 0$ half space is asymptotically, for large values of $\bar{\nu}r$

$$U(\theta, \rho, y, \bar{\nu}) \sim \left[B_i\left(\theta, \frac{y}{r}, \bar{\nu}\right) + \right.$$

$$\left. \int ds_\theta B_i\left(s_\theta, \frac{y}{r}, \bar{\nu}\right) \alpha\left(\theta - s_\theta, \frac{y}{r}, \bar{\nu}\right)\right] \frac{e^{i2\pi\bar{\nu}r}}{r} \quad (21)$$

The calculation of fields over all space has been described in this paper. However, if one is interested only in the field many wavelengths from the fiber it is necessary only: to define the illuminating field (e.g., by eq 5), the diameter of the fiber and the refractive index; to calculate the coefficients $a(m, s_y, \bar{\nu})$ by eq 17; to evaluate $\alpha(s_\theta, s_y, \bar{\nu})$ via eq 20; and to evaluate eq 21 to get the resulting far-field amplitude distribution.

The detection optics accept light over some entrance aperture surface $\mathcal{S}$ and the spectrometer resolves the wavenumber $\bar{\nu}$. In general, the field on the detection aperture must be mapped to the detector to determine the measured optical intensity. However, many common optical detection arrangements are well-approximated by modeling the detection process as an integration of the optical intensity over the detection aperture.[20] The detected intensity is then

$$I(\bar{\nu}) = \int_{\mathcal{S}} |U(\theta, \rho, y, \bar{\nu})|^2 dS$$

(22)

(25) Carney, P. S.; Wolf, E.; Agarwal, G. S. *J. Opt. Soc. Am. A* **1997**, *14*, 3366–3371.
(26) Mandel, L. Wolf, E., *Optical Coherence and Quantum Optics*, Chapter 3.3; Cambridge University Press: New York 1995; pp 350–355.
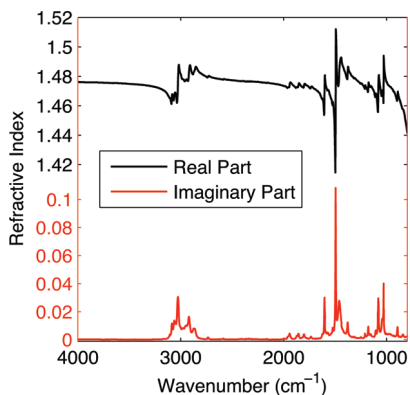
Figure 3. The complex refractive index of toluene.

Figure 4. Data predicted for toluene fibers of radii 5 and 10 μm, and for an ideal sample, of thickness $d = 10$ μm, exhibiting no optical artifacts. (a) The transmission fraction $I_S(\bar{\nu})/I_0(\bar{\nu})$. (b) The absorbance $A(\bar{\nu}) = -\log_{10}[I_S(\bar{\nu})/I_0(\bar{\nu})]$. For the ideal sample the absorbance is related to the imaginary refractive index by $A(\bar{\nu}) = 4\pi\bar{\nu}k(\bar{\nu})d/\log_{10}e$, whereas for the fibers the model presented here describes the more complicated relationship between the physical parameters of the fiber and the data.

For the remainder of this paper, it will be assumed that the detection optics consist of a detection Cassegrain opposing the illumination Cassegrain. The Cassegrain pair are matched in both focal point and aperture extent. It is also assumed that the common focal point of the Cassegrains lies at the center of the fiber.

A background measurement $I_0(\bar{\nu})$ is typically taken with no sample present between the Cassegrains. This signal depends both on the spectrum of the source and the optical characteristics of the measurement system. The measurement taken with the sample present will be denoted by $I_S(\bar{\nu})$. Ideally, the recorded absorbance is related to the absorption of the sample by,

$$A(\bar{\nu}) = -\log_{10}\left[\frac{I_S(\bar{\nu})}{I_0(\bar{\nu})}\right]$$

$$= \frac{4\pi\bar{\nu}k(\bar{\nu})d}{\log_e(10)} \quad (23)$$

where d is the thickness of the sample. However, even for relatively simple planar samples, this approach can be subject to significant errors due to diffraction, scattering and other optical effects.[20] This problem is even more significant in fiber measurement, where fiber radii are often of the order of the wavelength, leading to significant scattering artifacts. As an example, data are predicted for hypothetical cylinders made from toluene. Toluene has a well characterized complex refractive index,[27] seen in Figure 3, which allows a rigorous prediction of the measurement. We have also used toluene in previous theory-related publications, hence though a fiber of toluene is physically unrealistic, use of the same material provides a basis for comparison between the spectral responses from uniform films and cylindrical objects. The transmittance $I_S(\bar{\nu})/I_0(\bar{\nu})$, and the corresponding absorbance values, calculated from the first line of eq 23, are plotted in Figure 4. Significant differences can be seen between the data predicted for the different physical arrangements.

As seen in Figure 4, the imaginary part of the refractive index, that is, the spectral absorption profile of the fiber material, strongly influences the data. However, phenomena other than absorption also affect the data. Scattering directs light away from the detection
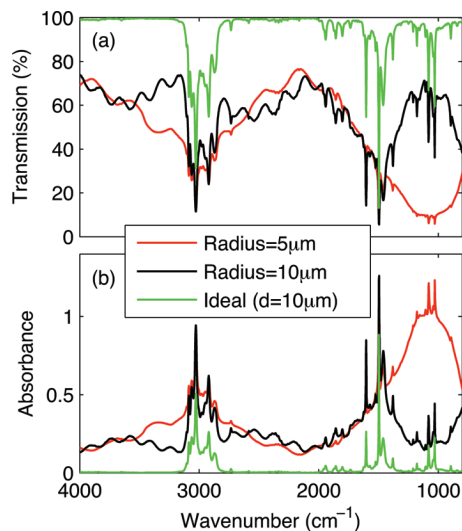
optics in a manner that depends both on the real part of the refractive index $n(\bar{\nu})$ and the radius of the fiber. The standard model presented in the second line of eq 23 is too simple to provide a quantitative understanding of the data. To measure the chemical absorption spectrum of the fiber material, it is necessary to use a rigorous physical model to extract the desired quantity, the imaginary part of the refractive index. The remainder of this manuscript describes a method for finding the imaginary index $k(\bar{\nu})$ from measured data.

INVERSE PROBLEM

A rigorous model was provided above for the interaction between the fiber and the focused probing light, that is, the measured spectrum can be predicted given a description of the fiber. This forward model must be inverted in order to recover the physical and true spectral properties of the fiber from the measurements. This inverse problem is solved by finding the fiber properties that best explain the measurements.

It is assumed that the fiber radius R can be independently measured, leaving the complex refractive index as the only unknown property of the fiber. Recovering the imaginary part of the index $k(\bar{\nu})$ is the primary goal, as a corrected absorbance profile can be calculated (see the second line of eq 23) from $k(\bar{\nu})$, that is, an absorbance function corrected for optical effects such as scattering. However, the real part of the refractive index $n(\bar{\nu})$ will also be determined as part of the solution to the inverse problem.

Finding the Constant Part of the Real Index. The real part of the refractive index necessarily varies in spectral regions exhibiting absorption, as quantified by the Kramers−Kronig relation.[28] However, in spectral regions exhibiting no absorption, the real index can be expected to be approximately constant. In

(27) Bertie, J. E.; Jones, R. N.; Apelblat, Y.; Keefe, C. D. *Appl. Spectrosc.* **1994**, *48*, 127–143.

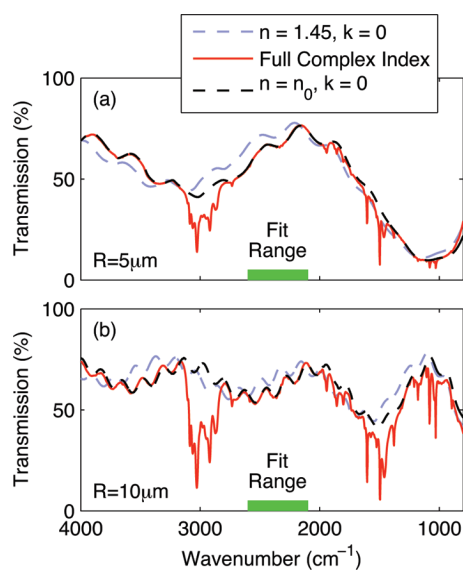(28) Toll, J. S. *Phys. Rev.* **1956**, *104*, 1760–1770.

Figure 5. Data predicted for fibers of (a) radius 5 μm and (b) radius 10 μm. Three fiber refractive indices are considered—a constant real index of $n = 1.45$, the complex index of toluene, and a constant real index found via a best fit procedure to the toluene data in the wavenumber range marked in green (2100 cm^{-1}—2600 cm^{-1}). The constant indicies n_0 are 1.477 for the 5 μm-radius fiber and 1.478 for the 10 μm-radius fiber.

the inversion procedure described here, a characteristic constant offset for the refractive index is assumed across the measurement bandwidth. This constant value, n_0, can be loosely regarded as the refractive index of the fiber absent any changes in the index produced by absorption peaks of the fiber material.

Most materials of interest exhibit a zero-absorbance zone between 2100 cm^{-1} and 2600 cm^{-1}. Within this range the refractive index will be real and slowly varying (see Figure 3). The value n_0 can be found by finding the real refractive index that best fits the data within this zero-absorbance band. Results of such a procedure are shown in Figure 5. It can be seen that a constant-index model fits the data well in regions of no absorption. It should also be noted that the estimated values of n_0 agree well between the two fibers, and are also consistent with the true index plotted in Figure 3.

The values of n_0 illustrated in Figure 5 were found via a simple one-dimensional optimization procedure. The merit of any candidate value of n_0 can be evaluated by calculating the mean square error between the $n(\bar{v}) = n_0$, $k(\bar{v}) = 0$ prediction and the data (in this case the simulated measurement from the toluene fiber). Minimizing this one-dimensional cost function gives the value of n_0. Here the golden section search[29] algorithm was used for minimization over the range $1 \leq n_0 \leq 1.8$. It should be noted that in general the goodness-of-fit will be a smooth continuous function, however local minima are to be expected. As the n_0 search space is one-dimensional and of limited range, convergence to local minima can be easily avoided. As illustrated by the $n = 1.45$ plots in Figure 5, the predicted data are sensitive to n_0, allowing a precise estimate to be made.

Recovering the Full Complex Index. The ultimate goal of this work is to find the complex refractive index of the fiber from measurements. The estimate of the complex index will be denoted

(29) Kiefer, J. *Proc. Am. Math. Soc.* **1953**, *4*, 502–506.

by $\hat{n}(\bar{v}) + i\hat{k}(\bar{v})$ and the corresponding predicted intensity will be written as $\hat{I}_S[\bar{v};\hat{n}(\bar{v}),\hat{k}(\bar{v})]$. The difference between the observed absorbance and the predicted absorbance can then be written as

$$E[\bar{v};\hat{n}(\bar{v}),\hat{k}(\bar{v})] = -\log_{10}\left\{\frac{I_S(\bar{v})}{I_0(\bar{v})}\right\} + \log_{10}\left\{\frac{\hat{I}_S[\bar{v};\hat{n}(\bar{v}),\hat{k}(\bar{v})]}{I_0(\bar{v})}\right\} \quad (24)$$

Looking at Figure 5, it appears that the data predicted for a real index of n_0 represent a baseline of the measurement. The error function $E[\bar{v};n_0,0]$ therefore represents a baseline corrected measurement. This sort of correction will be applied iteratively in an algorithm that reconstructs the complex refractive index of the fiber. Letting a bracketed superscript indicate the iteration number, the algorithm is

Initialize Set the initial index estimate to $\hat{n}^{(0)}(\bar{v}) = n_0$ and $\hat{k}^{(0)}(\bar{v}) = 0$. Initialize the iteration counter $j = 0$.

Predict Calculate the predicted data $\hat{I}_S^{(j)}[\bar{v};\hat{n}^{(j)}(\bar{v}),\hat{k}^{(j)}(\bar{v})]$.

Difference Evaluate the error function $E^{(j)}[\bar{v};\hat{n}^{(j)}(\bar{v}),\hat{k}^{(j)}(\bar{v})]$ using eq 24.

Update 1a Update the imaginary part of the complex refractive index as

$$\hat{k}^{(j+1)}(\bar{v}) = \hat{k}^{(j)}(\bar{v}) + \frac{\gamma}{\bar{v}}E^{(j)}[\bar{v};\hat{n}^{(j)}(\bar{v}),\hat{k}^{(j)}(\bar{v})] \quad (25)$$

where γ is a positive constant.

Update 1b Set any negative values of $\hat{k}^{(j)}(\bar{v})$ to zero.

Update 2 Update the real part of the complex refractive index as

$$\hat{n}^{(j+1)}(\bar{v}) = n_0 + \mathcal{K}[\hat{k}^{(j+1)}(\bar{v})] \quad (26)$$

where $\mathcal{K}$ is a transformation based on the Kramers−Kronig relation.

Iterate Increment the iteration counter, $j \leftarrow j + 1$, and either return to the **Predict** step or terminate if the algorithm has converged.

The algorithm is initialized with the real refractive index calculated in above. In each step a prediction of the data is made for the current estimate of the complex index. The absorbance corresponding to this prediction is compared to the measured absorbance and the difference is used to update the estimate of the imaginary index. As shown in eq 23, there is a $\bar{v}$ scaling relating the imaginary index and the absorbance. This scale factor appears in the update described in eq 25. The constant γ controls how much consecutive estimates of the imaginary index may differ. This constant should be positive to ensure that underpredicting the absorbance results in increasing the imaginary index. If γ is small, small updates will be made to the refractive index. This may result in slow convergence but also a more stable algorithm than for a large value of γ. The value suggested here is
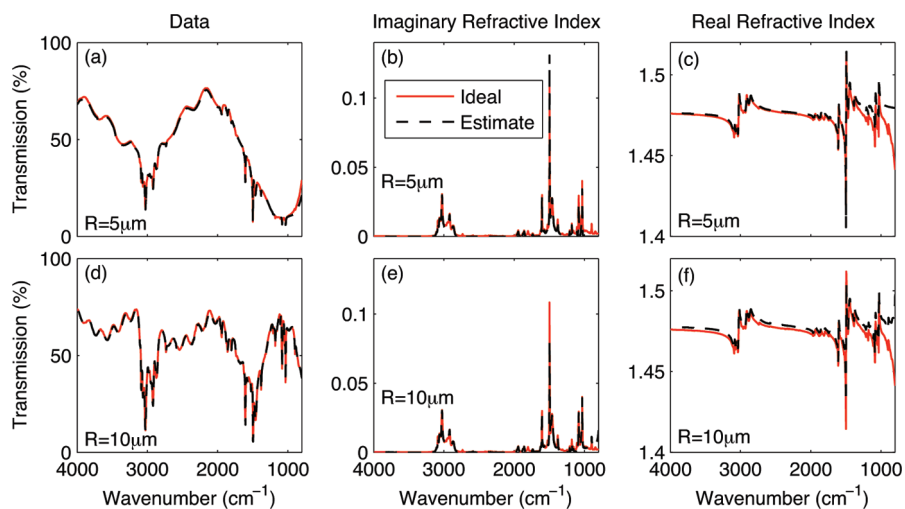
$$\gamma = \frac{\log_e(10)}{4\pi(2R)} \quad (27)$$

Figure 6. Reconstructions and true values of the complex refractive index and the corresponding predicted data. Fibers of radius 5 μm (a–c) and 10 μm (d–f) are considered. The transmission percentage is illustrated (a,d), along with the imaginary (b,e) and real (c,f) parts of the refractive index. The reconstructions shown were produced after nine iterations of the algorithm.
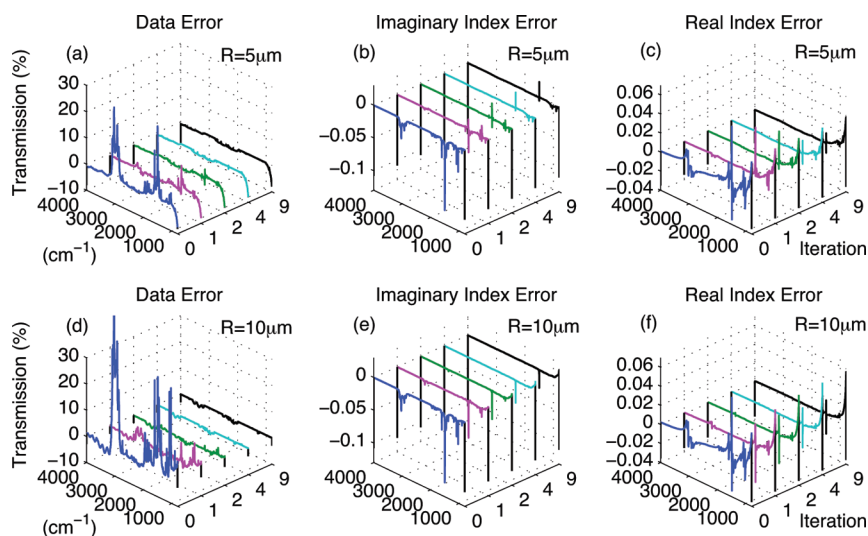

Figure 7. Differences between the estimated quantities and the true values as a function of iteration number. Data for fibers of radius 5 μm (a–c) and 10 μm (d–f) are shown. Differences are calculated for the transmission fraction (a,d), and the imaginary (b,e) and real (c,f) parts of the refractive index.

This value is motivated by considering eq 23 and an ideal planar sample with a thickness equal to the maximum thickness of the fiber (2R). The absorbing volume for the fiber will be less than the absorbing volume for this hypothetical planar sample, ensuring that γ is conservatively set. However, the physically motivated value of γ suggested in eq 27 will also be of approximately the correct order, leading to a rapidly converging algorithm.

Once the absorbance error has been used to update the imaginary index, any negative values of the result are set to zero. This is because a negative imaginary index is nonphysical, corresponding to optical amplification. Once the estimate of the imaginary index has been updated, the real index can also be updated. Using an algorithm[30] based on the Kramers–Kronig relation, the real index can be calculated from the imaginary index. Note that the Kramers–Kronig relation does not constrain the

constant component of the real index, and so the value n_0 is enforced explicitly.

The algorithm described above was applied to the data seen in Figure 4, which were calculated on an axis with a sample spacing of 2 cm^{-1}. The results are shown in Figure 6. It can be seen that the algorithm results in a refractive index estimate giving a close match between the measurement and the predicted data. The estimate of the index mostly follows the true value, but with some noteworthy departures.

The differences between the estimated quantities and the true underlying values are shown in Figure 7. It can be seen that the algorithm converges rapidly to a small error profile. The final mismatch between the prediction and the data (illustrated in plots (a) and (d) of Figure 7) is small, indicating that a feasible estimate of the refractive index has been found. However, it can also be seen that the estimated index does differ from the true value in a few key areas-most notably near the low-wavenumber edge of the axis and at the strongest absorption peak.

(30) Kuzmenko, A. B. *Rev. Sci. Instrum.* **2005**, *76*, 083108.

The departure near the edge of the axis can be explained by the nonlocal nature of the Kramers−Kronig relation. It is well-known that each value of the real index estimated by a Kramers−Kronig procedure is affected by a significant region of the spectral profile of the imaginary index.[30] This results in difficulty estimating the real index near the edge of the measurement bandwidth, as contributing imaginary-index regions are unobserved. This problem is borne-out in the example shown here, as a strong absorption band below the measurement bandwidth contributes to the real-index profile at the low-wavenumber region of the measurement. This kind of error may be corrected if prior knowledge of the refractive index outside the measurement band is available. It should also be noted that this error is less significant in the estimate of the imaginary index, which is all that will typically be of interest in absorption spectroscopy applications.

The estimate of the imaginary index also contains a significant error at the strong absorption peak at $\bar{\nu} = 1496$ cm^{-1}. High absorption peaks are necessarily associated with large changes in the real refractive index, which will in turn correspond to rapid changes in the scattering from the fiber. Consequently, at strong peaks it may be difficult to distinguish strong scattering from strong absorption. However, the algorithm does consistently distinguish these effects at lower absorption levels. It is also worth noting that the sign of the error at $\bar{\nu} = 1496$ cm^{-1} differs between the 5 μm-radius and the 10 μm-radius fibers.

SUMMARY AND OUTLOOK

In conclusion, we have shown that the molecularly specific spectral response of the constituent material of fibers is signifi-cantly distorted by the shape-dependent effects of scattering and refraction by the fiber itself. These results are important and applicable in the spectroscopic analysis of isolated fibers of a radius on the order the wavelengths considered. For fibers considerably smaller than the wavelength,[31] conventional spectral measurements on collections of fibers may be appropriate. For close-packed bundles of fibers in which the fibers cannot be considered isolated, these results may be generalized by extending the framework of the forward model proposed here with a T-matrix approach.[32]

A method for recovering the optical properties of the fiber (as characterized by the complex refractive index) from focused spectroscopic measurements was also developed. That is, we have presented a method of solving the inverse problem. This inverse solution makes possible geometry-independent spectroscopic characterization of optical fibers. In our implementation, a simplification was introduced in that the position and size of the fiber were known independently. These parameters could instead be jointly estimated along with the bulk spectral response similar to the approach taken in the analysis of nanoparticles.[33] With a diversity of polarization states incident and polarization-sensitive measurement, it is possible to include in this approach the estimation of birefringent susceptibilities. The framework proposed here forms the basis for such an extension.

(31) Kakade, M. V.; Givens, S.; Gardner, K.; Lee, K. H.; Chase, D. B.; Rabolt, J. F. *J. Am. Chem. Soc.* **2007**, *129*, 2777–2782.
(32) Mishchenko, M. I.; Travis, L. D.; Mackowski, D. W. *J. Quant. Spectrosc. Radiat. Transfer* **1996**, *55*, 535–575.
(33) Davis, B. J.; Carney, P. S. *J. Opt. Soc. Am. A* **2008**, *25*, 2102–2113.